

<https://doi.org/10.1038/s42005-025-02032-1>

Unidirectional focusing for broadband Lamb guided wave based on mode conversion

Haifei Zhu¹, Xuan Zhang¹, Wenjie Liu¹, Houyou Long¹✉, Ying Cheng^{1,2}✉ & Xiaojun Liu^{1,2}✉

Metamaterials promise to revolutionize elastic devices, with applications spanning wireless communication, structural health monitoring and microfluidic technology. Nevertheless, unidirectionally manipulating broadband elastic waves remains challenging due to their inherent complexity of polarization. Here, we introduce a method to control the transmission of broadband Lamb waves unidirectionally by utilizing mode conversion and selection. The elastic meta-atoms showcased >30 dB contrast in transmissions between forward and backward illumination scenarios within 251–345.9 kHz. Leveraging the disparity in phase velocities between S_0 - and A_0 -mode Lamb waves, the meta-atom enables broadband phase modulation. We realize a unidirectional focusing lens that exhibits a concentration of out-of-plane displacements for S_0 -mode Lamb waves under forward excitation, while reflecting those excited backward. An enhanced unidirectionally-transmitted meta-atom displaying <3 dB forward transmission within 293.3–333.6 kHz is further developed by incorporating an A_0 -mode reflector. Our proposal advances the manipulation of broadband plate waves, holding significant potential for multifunctional on-chip elastic devices.

Artificial metamaterials, which can exceed the constitutive parameters scope accessible by natural materials, hold the potential to exhibit exotic phenomena^{1–6}. These effects include anomalous refraction^{7–12} and super-resolution imaging^{13–15}, achieved by arranging meta-atoms to match desired phase profiles derived from the generalized Snell's law (GSL)¹⁶. Elastic metamaterials, in particular, have garnered considerable interest for manipulating plate waves extensively used in applications such as structural health monitoring¹⁷, energy harvesting¹⁸, and wireless communication¹⁹. For instance, Zhu et al. proposed a geometrically tapered metasurface and demonstrated anomalous refraction of elastic guided waves²⁰. Through mode conversion between S_0 and A_0 mode Lamb waves, manipulating only π phase shifts are required by adjusting the mass attachment height, with the remaining adjustments facilitated by mirror symmetry. Lee et al. introduced a method to disrupt intrinsic density-stiffness relationships by exclusively manipulating effective mass and stiffness, which facilitates the design of high transmission and a 2π phase range²¹. Additionally, various techniques involving zigzag beams for altering wave propagation paths^{22–25}, meta-gratings utilizing dispersion characteristics of elastic wave^{26,27}, and resonant pillar structures^{28–31} have been developed for anomalous manipulation of elastic wavefronts.

Among them, elastic-wave focusing has attracted paramount attentions for its potential applications in energy harvesting³² and nondestructive

testing³³. However, current elastic-wave focusing lenses exhibit bidirectional characteristics, lacking unidirectional focusing capabilities essential for multifunctional requirements in applications such as accurately identifying and extracting guided wave signals in non-destructive testing³³. A recent proposal for implementing a unidirectional focusing lens (UFL) for airborne sound involved dual-layer acoustic metasurfaces^{34,35}. While this mechanism is universal, suggesting potential for realizing a UFL for elastic waves, the forward focusing necessitates split beams by the first layer that converge into a spot by the second layer, which inevitably decreases focusing efficiency^{34,35}. Additionally, the dual-layer structure increases the complexity of the focusing lens. Moreover, while various elastic meta-structures have been proposed to manipulate Lamb waves, many of them suffer from narrow operating bandwidth and complex phase modulation methods^{32,33,36,37}.

To this end, we have put forth a method for implementing broadband unidirectional focusing of Lamb waves based on a single layer of unidirectionally-transmitted elastic meta-atoms (UTEM). A UTEM is composed of asymmetric grooves (AG) responsible for mode converter²⁰ and symmetric grooves (SG) acting as a mode selector. The mode converter transforms Lamb waves from the lowest-order symmetric (S_0) mode to the lowest-order asymmetric (A_0) mode, while the mode selector exhibits high transmission for A_0 -mode waves and high isolation for S_0 -mode waves.

¹Department of Physics, MOE Key Laboratory of Modern Acoustics, Collaborative Innovation Center of Advanced Microstructures, Jiangsu Physical Science Research Center, Nanjing University, Nanjing, China. ²State Key Laboratory of Acoustics, Institute of Acoustics, Chinese Academy of Sciences, 100190 Beijing, China. ✉e-mail: longhouyou@nju.edu.cn; chengying@nju.edu.cn; liuxiaojun@nju.edu.cn

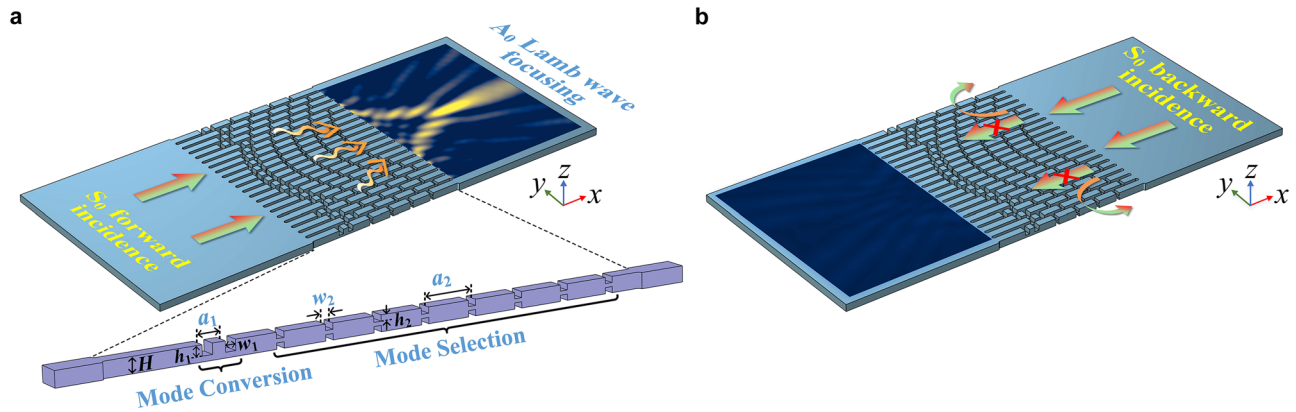


Fig. 1 | Schematics of a unidirectional focusing lens (UFL). **a** Forward incident S_0 -mode Lamb waves are converted into A_0 -mode waves and focused on the right side of the lens. Inset: 3D view of a unidirectionally-transmitted elastic meta-atom (UTEM) composed of a mode converter and a mode selector, respectively. The

geometric parameters a_1 (a_2), w_1 (w_2), and h_1 (h_2) correspond to the periodicity, width, and depth of the asymmetric groove (symmetric groove), while H represents the plate thickness of the UTEM. **b** Backward incident S_0 -mode Lamb waves are largely unable to transmit to the left side.

Consequently, the forward incident S_0 -mode Lamb waves are converted into transmitted A_0 -mode waves by the mode converter, enabling unidirectional transmission, as waves from the opposite direction are reflected by the mode selector. The forward-backward transmission difference exceeds 30 dB between 251 kHz and 345.9 kHz (relative bandwidth of 31.8%). Moreover, we propose a method to adjust the transmitted phases of the UTEM for broadband Lamb waves by leveraging the substantial phase velocity difference between Lamb waves in S_0 and A_0 modes. Based on this approach, we have developed and tested a broadband UFL demonstrating unidirectional focusing through numerical simulations and experiments using a laser vibrometer system. Furthermore, we introduce an enhanced UTEM showing <3 dB (<37 dB) transmission spectrum in the forward (backward) direction within the frequency range of 293.3 kHz to 333.6 kHz. At transmission peaks, 0 dB transmission spectrum is achieved, indicating that the reflection of A_0 -mode Lamb waves compensates for the low transmission resulting from the inherently low conversion efficiency²⁰. On this basis, we design an enhanced UFL with improved elastic-wave unidirectional focusing characteristics verified through numerical simulations.

Methods

Unidirectional Lamb-wave focusing lens

A schematic illustration of the proposed UFL is presented in Fig. 1. In the forward direction, S_0 -mode Lamb waves lead to a focal point of converted A_0 -mode Lamb waves on the right side of the lens (Fig. 1a). Conversely, backward-propagating waves are predominantly reflected (Fig. 1b), as an S_0 -mode band gap prevents their transmission, resulting in unidirectional focusing. The broadband unidirectional focusing capabilities are enabled by UTEMs that serve the dual functions of mode conversion and phase modulation. Specifically, (1) a UTEM, shown in the inset of Fig. 1, converts forward-propagating S_0 -mode Lamb waves into A_0 mode through the AG while blocking backward transmission by the SG's forbidden band of S_0 -mode Lamb waves, ensuring unidirectional transmission. (2) Furthermore, a UTEM exhibits the capacity to manipulate the phase of broadband Lamb waves. The phase shifting of the UTEM arises from the disparities in phase velocities between S_0 and A_0 Lamb waves, implying that phase modulation is independent of the UTEM's geometry but rather relies on the placement of the mode converter, as discussed in detail later.

In this study, the UTEM is constructed from single-phase aluminum material with a mass density of 2700 kg/m³, Poisson's ratio of 0.33, and Young's modulus of 70 GPa. The geometric parameters a_1 (a_2), w_1 (w_2), and h_1 (h_2) represent the periodicity, width, and depth of the asymmetric (symmetric) grooves, respectively, while H denotes the thickness of the plate (see Supplementary Table 1 in Supplementary Note 1). Here, the interval between the AG and the SG is optimized at 6.5 mm (see Supplementary Note 1). Although the UTEM consists of two sub-structures (the AG and the

SG), it functions as a local diffractive meta-atom within the UFL. The interval between the AG and the SG primarily governs the transmission efficiency of a diffraction meta-atom, which is fundamentally different from the interval that establishes the nonlocal interconnection between dual-layer metasurfaces in the reference³⁵. The lateral width of the UTEM is 2 mm, slightly narrower than its 3 mm period, thereby preventing coupling between adjacent UTEMs in a UFL.

Design of a broadband UTEM

Due to its non-symmetric configuration across the mid-plate, an AG can disrupt the displacement symmetry of the S_0 -mode Lamb wave²⁰. To illustrate this conversion process, a time-domain analysis was performed using COMSOL Multiphysics software. The probed displacement packet on a cut line of the surface of the AG is depicted in Fig. 2a, with the red solid line and blue short dashed line indicating out-of-plane (denoted as w) and in-plane (denoted as u) displacements, respectively. Although the displacements u and w on the surface of the AG appear to have comparable amplitudes, the energy is dominantly carried by the out-of-plane displacement (see Supplementary Note 2). The significant disparity in phase velocities between Lamb waves in the A_0 (2059 m/s) and S_0 (5360 m/s) modes enables the differentiation of wave packets related to the converted A_0 mode and the residual S_0 mode. Therefore, the frequency spectra of the transmitted wave packets are derived to quantitatively characterize their transmission spectra as $10\lg[(u^2 + w^2)/(u_0^2 + w_0^2)]$ ³⁸, where u_0 and w_0 represent the displacement components of the plate without AG. As shown in Fig. 2b, an approximately 3 dB transmission spectrum is achieved (calculated based on the converted A_0 -mode Lamb wave) within the frequency range of 250 kHz to 350 kHz (a relative bandwidth of 33%), indicating a potential conversion efficiency of 50% within the observed frequency band. Here, the optimal height of the AG is set to 1.33 mm, which results from a trade-off between the transmission and reflection of the S_0 -mode Lamb wave (see Supplementary Note 3). Moreover, it has been observed that the conversion efficiency decreases with an increasing number of AGs, leading to a higher reflection of the converted A_0 mode (see Supplementary Note 3).

On the other hand, the SGs function as a mode selector, allowing Lamb waves in the A_0 mode transmitting through while blocking those in the S_0 mode. To maximize the operating bandwidth while ensuring unidirectional performance of the UTEM, the band structures of the SG with varying height h_2 are derived. The optimal height h_2 is found to be 0.75 mm (see Supplementary Note 4). This configuration enables a passing band for A_0 -mode Lamb waves, spanning the range from 254 to 341 kHz, within the bandgap of S_0 -mode Lamb waves (252 to 460 kHz), as illustrated in Fig. 2c. Additionally, the transmission spectra of the SGs for Lamb waves in both A_0 and S_0 modes have been calculated, as shown in Fig. 2d. To configure the mode selector, 8 pairs of SGs were utilized, as further enhancement of

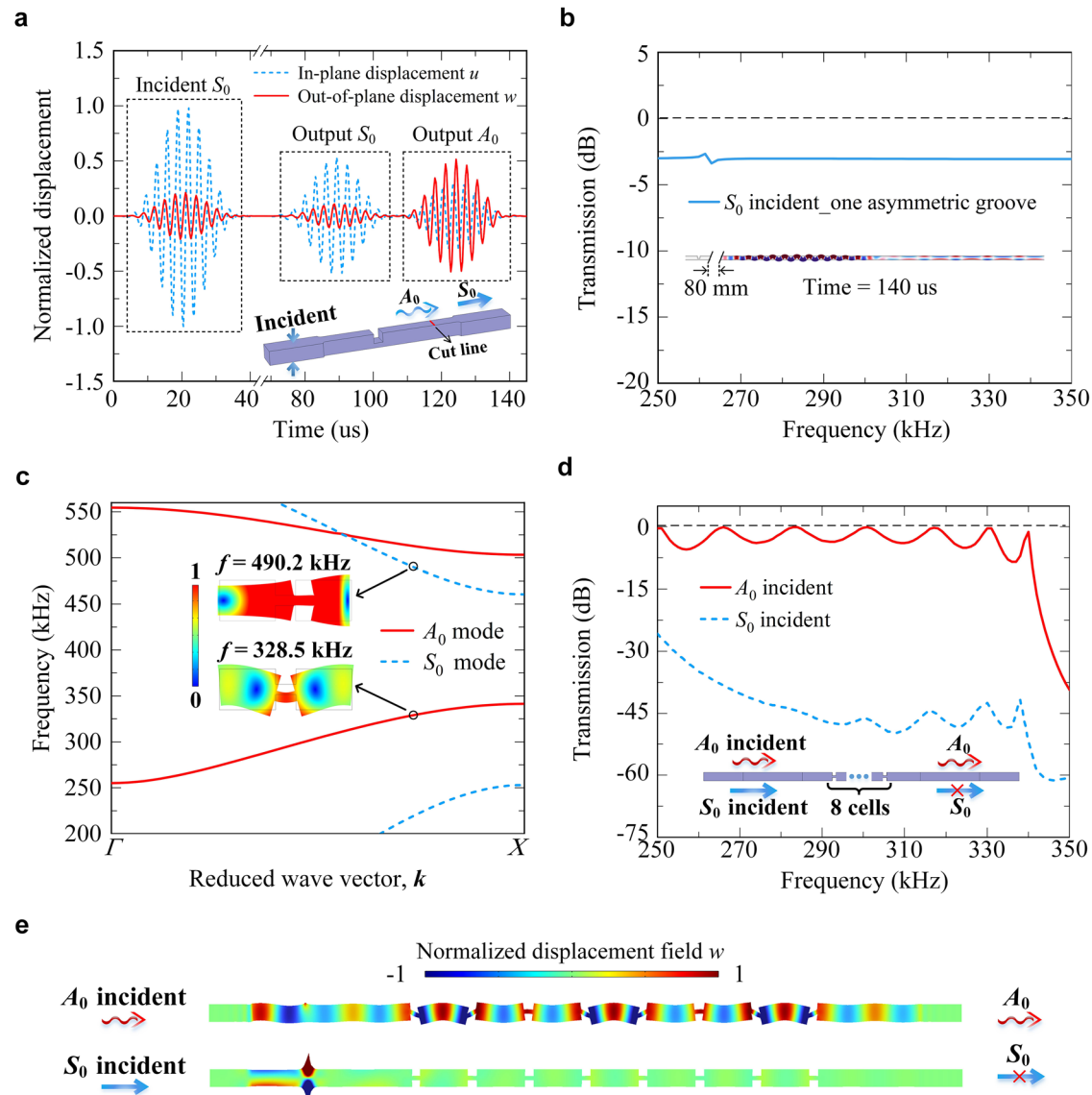


Fig. 2 | Transmission characteristics of the asymmetric groove (AG) and the symmetric grooves (SGs). **a** Time-domain wavefront of S_0 -mode Lamb wave propagating in a plate with an AG, as schemed by the inset. The blue short dashed and red solid lines denote for the in-plane and out-of-plane displacements, respectively. **b** Transmission spectrum of the AG for A_0 mode. The inset shows the displacement distribution at 55 μ s. **c** The band structure of the SG, where the insets show the total

displacement at 490.2 kHz and 328.5 kHz, respectively. The red solid line and blue short dashed line, respectively, represent the energy bands of the SG for A_0 - and S_0 -mode Lamb waves. **d** The transmission spectra of incident S_0 (blue short dashed line) and A_0 (red solid line) modes wave passing through the SG. **e** Out-of-plane displacements of A_0 - and S_0 -mode Lamb waves at 320 kHz.

transmission difference between forward and backward incidents becomes challenging with more than 8 SGs (see Supplementary Note 5). In the numerical simulations, perfectly matched layers were employed on both sides to eliminate the interference of reflected waves. Figure 2d demonstrates that transmission spectrum is maintained below 5 dB for A_0 modes and above 30 dB for S_0 modes within the frequency range of 259 kHz to 334 kHz. The transmission ratio consistently exceeds 30.6 dB at each frequency. At 320 kHz, Fig. 2e shows the out-of-plane displacement distributions of the two modes, confirming the SGs' function as an effective mode selector.

Therefore, the S_0 -mode Lamb wave initially excited from the left side of the UTEM (see inset in Fig. 1) undergoes conversion into the A_0 mode and is subsequently transmitted to the right side. Conversely, the S_0 -mode Lamb wave originating from the right side experiences almost complete reflection by the SGs, leading to unidirectional transmission. To verify this, transmission spectra of the UTEM comprising of an AG and eight SGs are calculated and presented in Fig. 3a, where the red solid line and the blue short dashed line represent the transmission spectrum in the

forward-incident and backward-incident scenarios, respectively (see Supplementary Note 5 for transmission spectra of the UTEM with varying number of AGs and SGs). The analysis reveals that within the frequency range of 251–345.9 kHz (a relative bandwidth of 31.8%), transmission spectrum remains below 10 dB for forward transmission and exceeds 30 dB for backward transmission. A transmission spectrum exceeding 30 dB is consistently achieved across the observed frequency range, as demonstrated in Fig. 3a. For instance, at 328.5 kHz, the transmission ratio reaches approximately 37.4 dB. Visually, the normalized out-of-plane displacements for forward and backward incidences are depicted in Fig. 3b, clearly illustrating unidirectional transmission. It is highlighted that in the backward-incident case, the S_0 -mode Lamb wave is reflected by the SGs, as indicated by the in-plane displacement (see Supplementary Note 6). The unidirectional transmission mechanism can be extended to higher frequencies, specifically in the MHz range, with the straightforward configuration applicable for constructing a UTEM on a silicon substrate (see Supplementary Note 7).

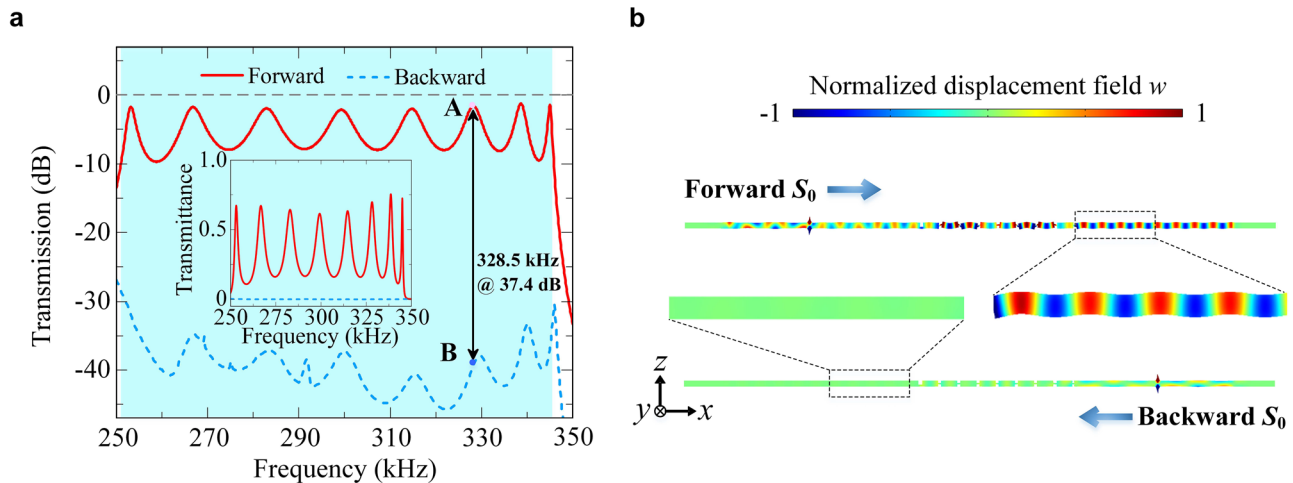
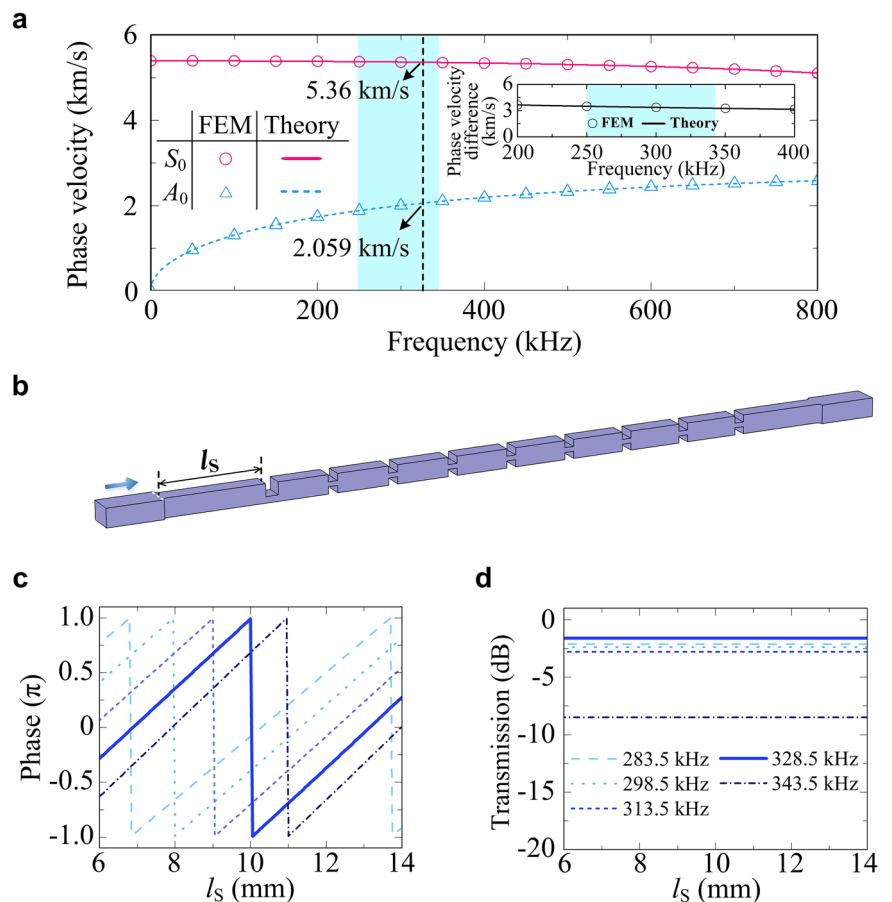


Fig. 3 | Transmission characteristics of the unidirectionally-transmitted elastic meta-atoms (UTEM). **a** Transmission spectra of the UTEM for forward- (red solid line) and backward-incident (blue dashed line) S_0 Lamb wave. The shaded area indicates the frequency range where forward transmission is below 10 dB while

backward transmission exceeds 30 dB. The inset presents corresponding transmittance. The legend of **a** refers to the inset. **b** Out-of-plane displacements of the UTEM when S_0 -mode Lamb wave at 328.5 kHz impinged from forward and backward directions, corresponding to points A and B in (**a**), respectively.

Fig. 4 | Phase modulation of the unidirectionally-transmitted elastic meta-atoms (UTEM).

a Dispersion curves for S_0 - (red solid line and circles) and A_0 -mode (blue short dashed line and triangles) Lamb waves on a 2 mm-thick aluminum plate. The shaded area indicates the operating frequency range. Inset: phase velocity difference between S_0 - and A_0 -mode Lamb waves. **b** Schematic diagram of a UTEM with the capability of broadband phase modulation. l_s denotes for the propagation length of S_0 -mode Lamb wave. **c** Transmission phases and **d** amplitudes as a function of l_s . The legend of **d** refers to (**c**).



Phase modulation of the UTEM

The availability of phase shifts that can be modified across a wide frequency range is crucial for steering Lamb waves. Nevertheless, current phase-modulated structures such as tapered torus²⁰ and resonant structures^{28–31} suffer from a limited operating band, while broadband phase-modulation units are less involved²⁷. Achieving high transmission and desired phases requires precise optimization of geometric

parameters, such as adjusting the height of the attached mass as discussed in literature²⁰. In this study, we propose an approach for modulating broadband Lamb waves by changing the position of the UTEM. This method leverages the phase velocity difference between Lamb waves in the S_0 and A_0 modes, contrasting with traditional methods that focus on adjusting the geometric configurations of a meta-atom^{20,28–31}.

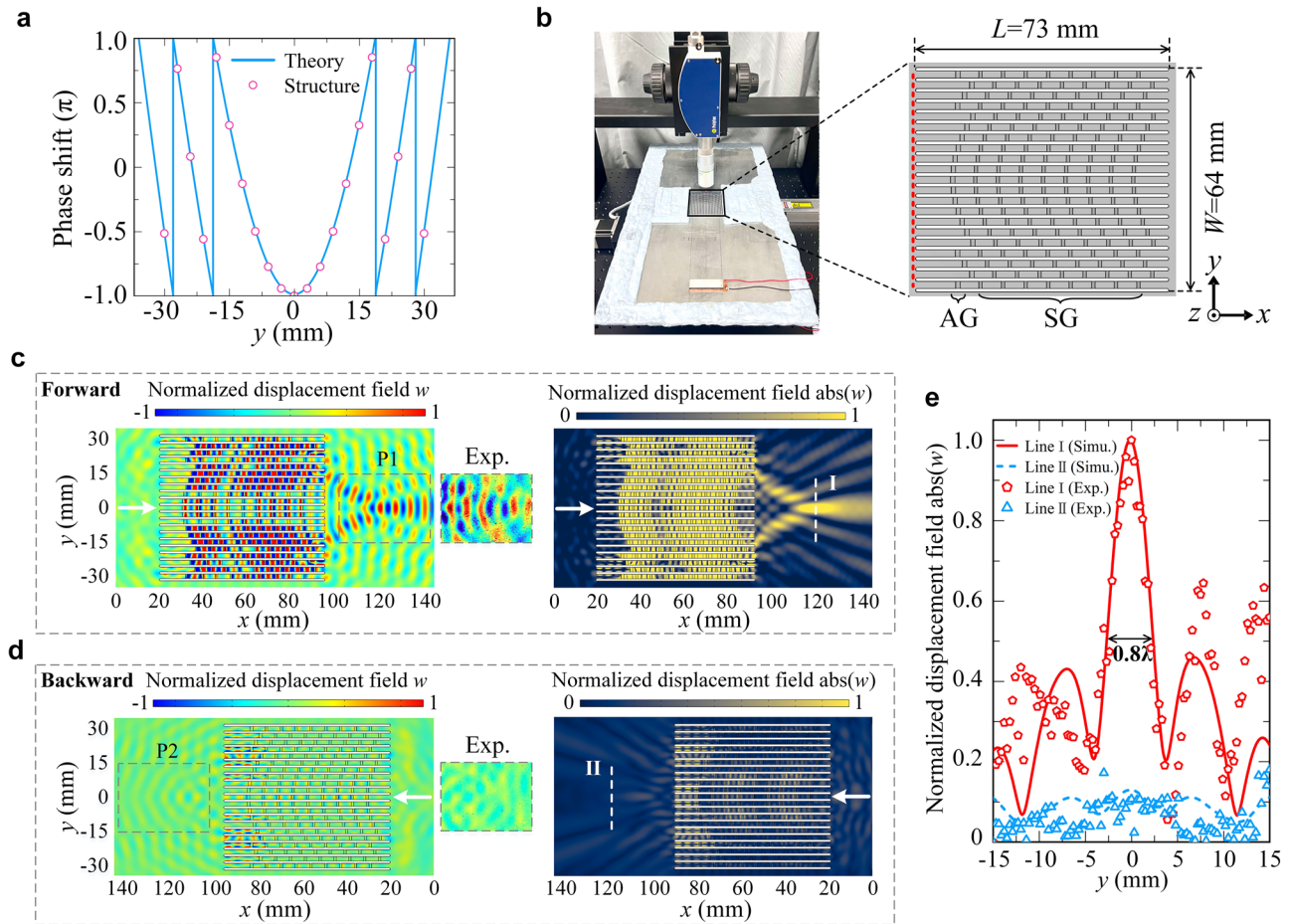


Fig. 5 | Numerical simulations and experimental illustrations of the unidirectional focusing lens (UFL). **a** Phase profile of the designed UFL, with the solid line representing the theoretical result from the generalized Snell's law and the symbols indicating that of the unidirectionally-transmitted elastic meta-atoms (UTEM). **b** Experimental setup for measuring out-of-plane displacements. Inset: The designed UFL consists of asymmetric groove (AG) and symmetric grooves (SGs), and the UFL

has a length $L = 73$ mm and width $W = 64$ mm. The simulated distributions of the displacement fields w (left panels) and the amplitudes $|w|$ (right panels) of the UFL in **c** forward- and **d** backward-incident cases at 328.5 kHz. The dashed-line boxes mark the measurement areas. The insets show the measured displacement field distributions. **e** Comparison of simulated (lines) and measured (hollow symbols) displacement field profiles along the white dashed lines I and II in (c) and (d).

We examine the phase velocity at various frequencies by solving the dispersion equation of the Lamb wave as described in ref. 39:

$$\frac{\tan(qH/2)}{\tan(pH/2)} = -\frac{4k^2qp}{(q^2 - k^2)^2}, \quad (1)$$

$$\frac{\tan(qH/2)}{\tan(pH/2)} = -\frac{(q^2 - k^2)^2}{4k^2qp}, \quad (2)$$

where Eqs. (1) and (2) correspond to the symmetric and asymmetric modes of the Lamb wave; $p^2 = \omega^2/c_L^2 - k^2$ and $q^2 = \omega^2/c_T^2 - k^2$, with c_L and c_T denoting the velocities of longitudinal and transverse waves, respectively. The obtained dispersion curve for a 2 mm-thick aluminum plate is depicted in Fig. 4a. A significant disparity in phase velocities between the S_0 - and A_0 -mode Lamb waves is evident within the specified frequency range of 251 kHz to 345.9 kHz, highlighted by the cyan shadow in Fig. 4a, where the inset compares the phase velocities. For instance, at 328.5 kHz, the phase velocities of the Lamb wave in the S_0 and A_0 modes are 5.36 km/s and 2.059 km/s, respectively. Consequently, the S_0 - and A_0 -mode Lamb waves exhibit distinct phase accumulations along the same propagation path, motivating us to adjust the phase by altering the propagation length of the S_0 mode (before conversion into the A_0 mode) or the starting position of the AG, as schemed in Fig. 4b. Here, the total length of the phase-modulating

UTEM is 73 mm, with the AGs and SGs occupying 53.2 mm. l_s represents the propagation length of the S_0 mode. Figure 4c, d demonstrates the transmission phases and amplitudes at various frequency points. It is worth mentioning that (1) the transmission phases are solely modulated by adjusting the initial position of the AG, simplifying the manufacturing process compared to tapered torus²⁰, zigzag structures^{22–25}, and resonant structures^{28–31,37}. (2) The transmission phases exhibit a linear variation with the propagation length at different frequencies, laying the foundation for steering broadband Lamb-wave focusing.

Results and discussion

Broadband unidirectional Lamb-wave focusing

In this section, we explore the potential of implementing a UFL based on the proposed UTEM technique. To achieve the focusing of the A_0 -mode Lamb wave, the gradient phase distribution profile along the y direction must satisfy the following relation according to the GSL:

$$\Phi(y) = \frac{2\pi}{\lambda} \left(\sqrt{F^2 + y^2} - F \right) + \Phi(y=0), \quad (3)$$

where the focal length $F = 4\lambda$ and $\lambda = 6.26$ mm denotes for the wavelength of the Lamb wave in A_0 mode at 328.5 kHz. Here, we set the phase $\Phi(y=0) = -\pi$. Accordingly, the requisite phase profile is depicted by the solid line in Fig. 5a. For the physical realization of the UFL, 21 UTEMs have been

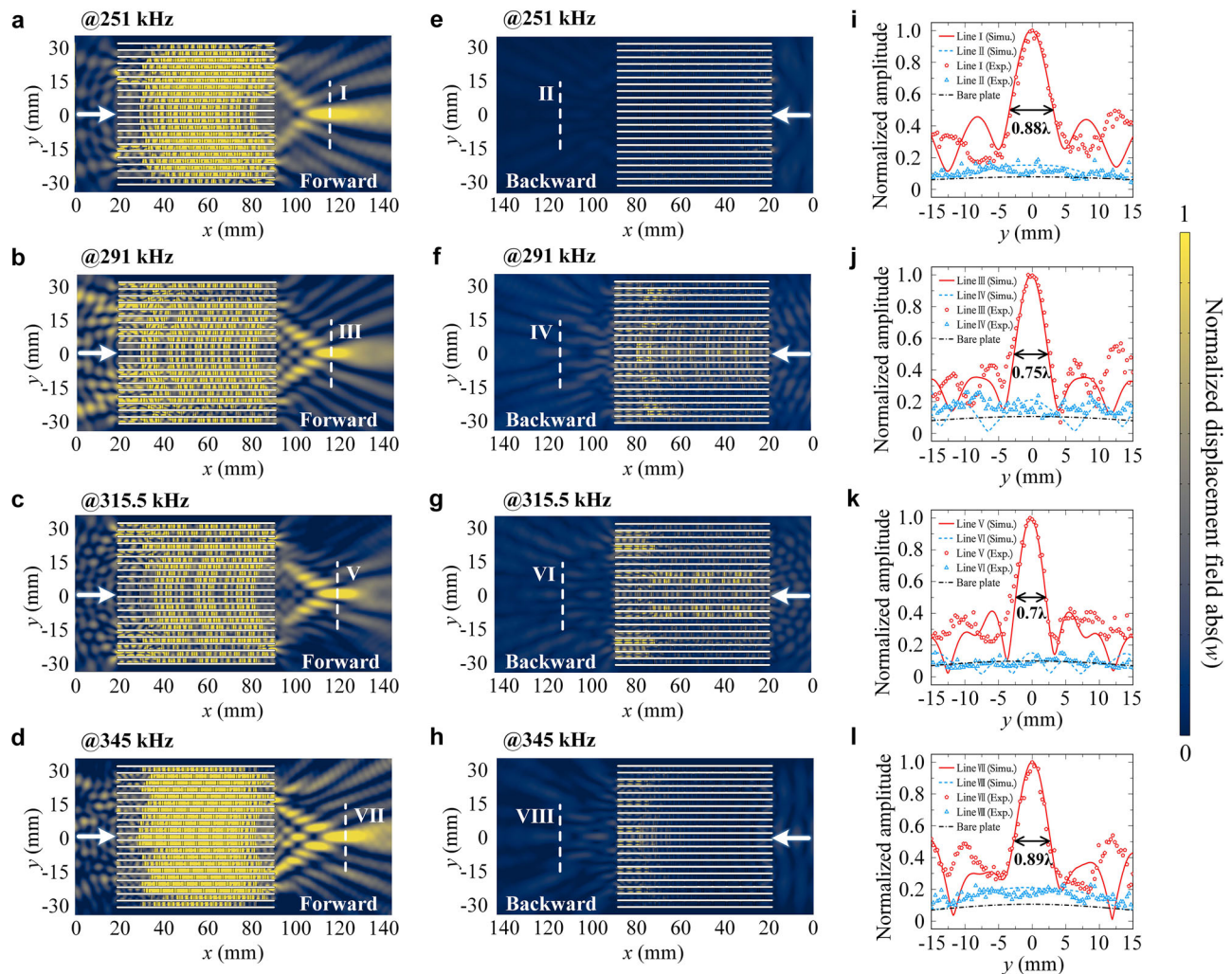


Fig. 6 | Unidirectional Lamb-wave focusing at different frequencies. Simulated displacement amplitudes in the forward (a–d) and backward (e–h) cases at frequencies of 251 kHz, 291 kHz, 315.5 kHz, and 345 kHz. Note that 291 kHz corresponds to the transmission valley of the unidirectionally-transmitted elastic meta-

atoms (UTEM). i–l are correspondingly simulated (lines) and measured (hollow symbols) displacement field profiles along the white dashed lines. For comparison, the normalized absolute amplitudes $|w|$ at the same position of a bare plate without any grooves are presented by black dash dotted lines.

employed, and their respective phases are indicated by symbols in Fig. 5a. The normalized out-of-plane displacements derived from the finite element method in both forward- and backward-incident scenarios are illustrated in Fig. 5c, d, respectively. Upon the illumination of the S_0 -mode Lamb wave in the forward direction, a focal point of out-of-plane displacements is observed on the opposite side of the UFL. This observation signifies the conversion of the in-plane dominated S_0 mode into an A_0 mode, focused precisely within the region specified by the phase profile (Fig. 5c). Conversely, minimal displacement is observed on the left side of the lens when the S_0 -mode Lamb wave is incident from the right side (Fig. 5d). This behavior is attributed to the direct reflection of the backward-incident wave by the UFL. Hence, the numerical simulation validates the unidirectional focusing characteristics of the UFL.

To experimentally validate the unidirectional focusing capabilities of the constructed UFL, a specimen was fabricated by using computer numerical control technology. Pointwise displacement detection was conducted using a laser vibrometer system (Polytec OFV-534 and OFV-5000), as illustrated in Fig. 5b. The fabricated lens was mounted on a displacement stage, controlled by a LabVIEW program to derive the pointwise displacement fields. The edges of the lens were affixed with blue tack glue to simulate a low-reflection boundary. The S_0 -mode Lamb wave was generated by a pair of piezoelectric patches attached to the aluminum plate on both faces. An electrical signal of 60 cycles was generated, amplified by a E&I

325LA power amplifier to enhance the signal-to-noise ratio. An OFV-5000 vibrometer controller was utilized to measure the out-of-plane displacement with a precision of 0.3 mm ($<1/6$ of the operating wavelength of 6.26 mm). The acquisition region P1 and P2 was $40 \times 30 \text{ mm}^2$, as outlined by the dashed line in Fig. 5c, d. The measured displacements are displayed in Fig. 5c, d, which agree well with those derived from the numerical simulation. The dynamic process of the measured displacements is presented in Supplementary Movie 1. The simulated and measured displacement field profiles along the white dashed lines I and II of Fig. 5c, d are presented in Fig. 5e. The full width at half maximum (FWHM) was observed to be 5 mm, approximately 0.8λ of the A_0 -mode Lamb wave at 328.5 kHz. We acknowledge that the non-contact detection technique employed has limitations, as it only measures out-of-plane displacements. While this measurement alone is insufficient to fully characterize the A_0 -mode Lamb wave, detecting out-of-plane displacements remain the most widely used approach due to their dominant role in A_0 -mode Lamb waves^{40,41}.

We note that although the UFL was precisely designed at 328.5 kHz, however, unidirectional focusing is observed over a broad frequency range from 251 to 345.9 kHz. Broadband focusing is facilitated by the linearly varying transmitted phase with respect to the modulated parameter l_s , along with its nearly linear gradients across different frequencies (see Fig. 4c). For further validation, we have also presented phase profiles of the designed UFL at different frequencies, which are distributed in a focusing lens

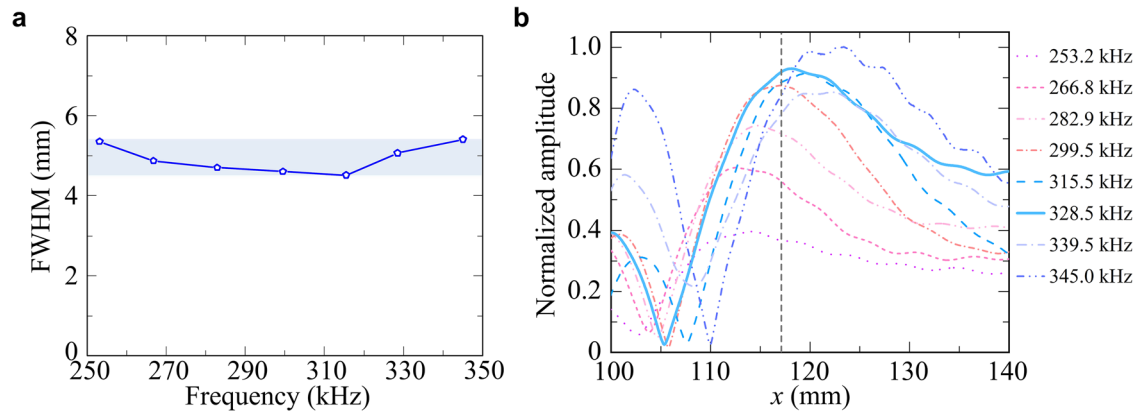


Fig. 7 | The broadband focusing performance of the unidirectional focusing lens (UFL). **a** The full width at half maximum (FWHM) of the UFL at 253.2 kHz, 266.8 kHz, 282.9 kHz, 299.5 kHz, 315.5 kHz, 328.5 kHz, and 345 kHz. The shaded

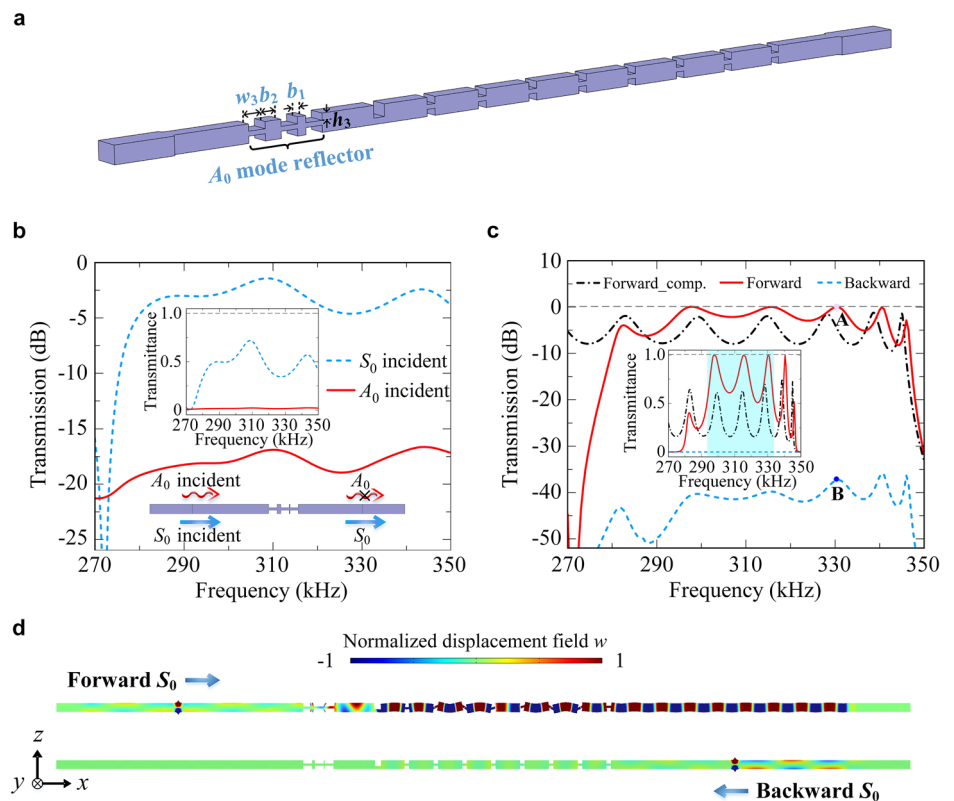
area indicates the subwavelength FWHM within 4.51–5.4 mm. **b** Normalized displacement field profiles of the UFL along x -direction, the black short dash lines denote the designed focal length $F = 25.04$ mm at 328.5 kHz.

Fig. 8 | Enhanced unidirectional transmission.

a Schematic diagram of the enhanced unidirectionally-transmitted elastic meta-atoms (EUTEM). The geometric parameters w_3 and h_3 correspond to the width and depth of the mode reflectors, respectively, while the b_1 and b_2 represent the interval between adjacent grooves.

b Transmission spectra of the reflector for S_0 -mode (blue short dashed line) and A_0 -mode (red solid line) Lamb waves. Inset: the corresponding transmittance. The schematic shows that the S_0 -mode Lamb waves can pass through the reflector while the A_0 -mode Lamb waves are reflected back.

c Transmission spectra of the EUTEM for forward (red solid line) and backward (blue short dashed line) incident S_0 -mode Lamb waves. Inset denotes for the corresponding transmittance. The shaded area indicates frequency ranges with enhanced forward transmission. The black dash dotted line denotes the transmission spectrum without reflector for comparison. **d** Out-of-plane displacement field of the EUTEM for forward and backward-incident S_0 mode at 330.5 kHz, corresponding to points A and B in (c), respectively.



configuration across the prescribed frequency range (see Supplementary Note 8). To maintain generality, we analyzed the out-of-plane displacement distributions at four specific frequencies: 251 kHz, 291 kHz, 315.5 kHz, and 345 kHz, as illustrated in Fig. 6. The measured displacements, represented by hollow symbols in Fig. 6i–l, closely align with those predicted by numerical simulation. The FWHM serves as a crucial metric for assessing focusing performance. The FWHMs at different frequencies are graphically presented in Fig. 7a, indicating that the UFL achieves sub-wavelength-scale FWHMs ranging from 4.51 mm to 5.4 mm, smaller than the minimum wavelength of 6.04 mm. Therefore, it is confirmed that the designed UFL exhibits good focusing resolution and broadband performance.

Additionally, the focusing effect is evaluated through an investigation of the focal lengths at various frequencies, as illustrated in Fig. 7b. The results indicate an increase in focal length with frequency, ranging from 21.7 mm to

29.7 mm, demonstrating the effective focusing capability of the constructed UFL across a wide frequency range from 251 kHz to 345.9 kHz. The shift in focal position along the x direction is attributed to the inherent dispersion of Lamb waves, as evidenced by the linear phase shifts observed in the UTEM at various frequencies. It is noteworthy that the designed frequency does not represent a singular solution. To confirm this, a UFL designed to operate at 298.5 kHz was fabricated, showing broad-spectrum unidirectional focusing characteristics (see Supplementary Note 9). Additionally, we highlight that the method can be extended to construct a UFL for broadband A_0 -mode Lamb waves. Specifically, the forward illuminated A_0 -mode Lamb waves undergo mode conversion into S_0 -mode waves, which are then focused onto the right side of the UFL. In contrast, A_0 -mode Lamb waves incident from the backward direction are effectively reflected by the mode selector (see Supplementary Note 10).

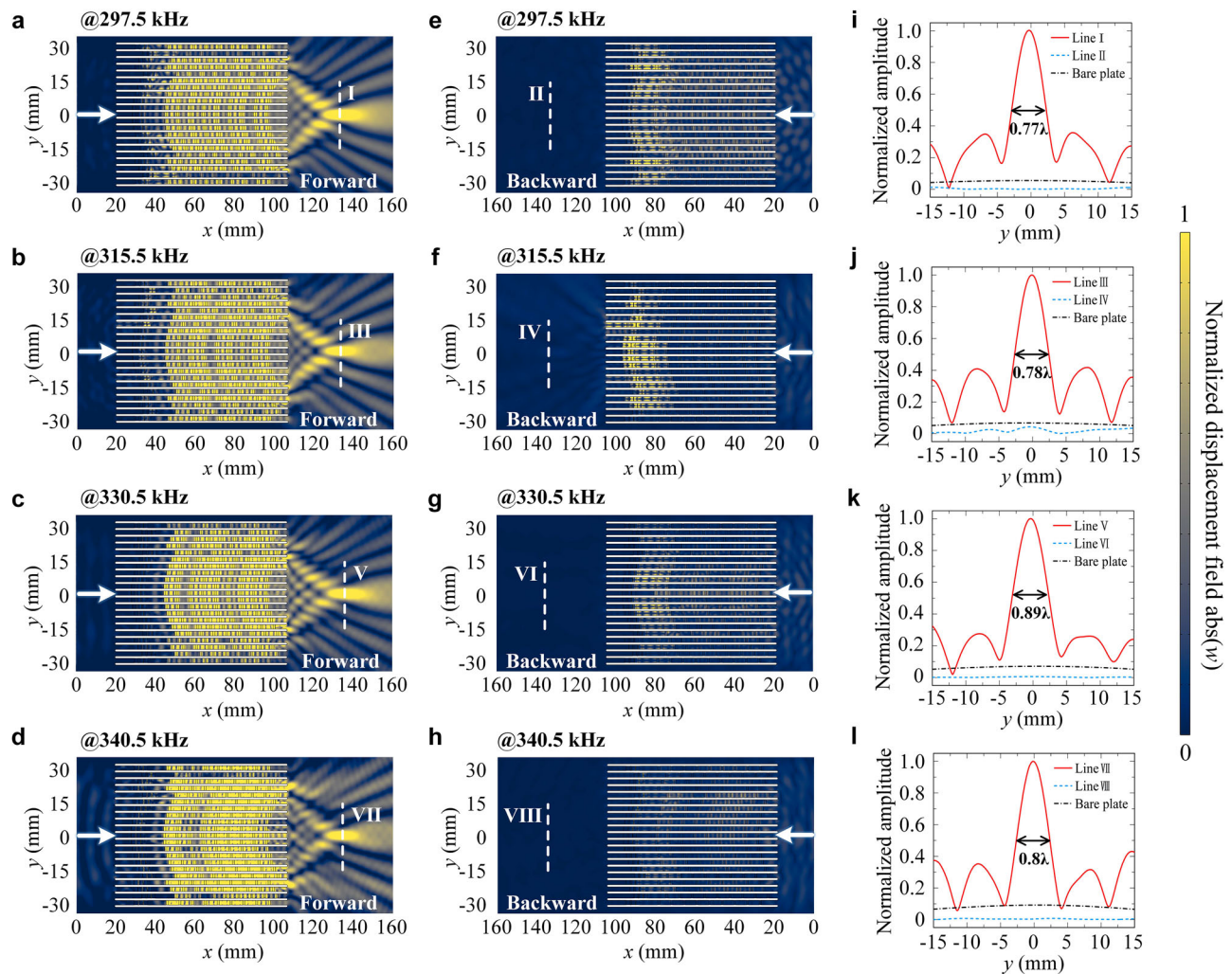


Fig. 9 | Enhanced unidirectional Lamb-wave focusing. Simulated normalized absolute out-of-plane displacements of the enhanced unidirectional focusing lens (EUFL) for forward (a–d) and backward (e–h) incidences at 297.5 kHz, 315.5 kHz,

330.5 kHz, and 340.5 kHz. i–l correspond to the normalized focusing amplitudes along the white dashed lines. The normalized amplitudes $abs(w)$ at the same position of a bare plate without any grooves are shown by the black dash dotted lines for comparison.

Enhanced unidirectional Lamb-wave focusing

The mode conversion between S_0 and A_0 results in a loss of transmission efficiency²⁰. Specifically, a mode converter transforms a portion of the Lamb wave from the S_0 mode to the A_0 mode, while the remaining part passes through the converter (refer to Fig. 2a) and is subsequently reflected by the SG elements, eventually reaching the impinged terminal (see Supplementary Movie 2). Consequently, the above-proposed UTEM exhibits an approximate 1.3 dB transmission spectrum even at peak transmission levels (see Fig. 3a).

To mitigate this issue, we propose a strategy to develop an enhanced unidirectionally-transmitted elastic meta-atoms (EUTEM) by incorporating a reflector for the A_0 -mode Lamb wave. As schemed in Fig. 8a, the reflector consists of three SGs, with geometric parameters w_3 and h_3 set at 2 mm and 0.75 mm, respectively, and $b_1 = 0.2$ mm, $b_2 = 0.64$ mm. The interval between the reflector and the mode converter is 11 mm (refer to Supplementary Note 11 for transmission spectra with different intervals). As depicted by Fig. 8b, the proposed reflector features high transmission (<5 dB) for Lamb waves in the S_0 mode but high reflection (<16.6 dB) for those in the A_0 mode within the frequency range of 279.5 kHz to 350 kHz. The EUTEM shows <3 dB transmission spectrum (<0.5 transmission coefficient as depicted in the inset) in the forward incidence scenario (red solid line in Fig. 8c) within the frequency range of 293.3 kHz to 333.6 kHz, showcasing significant transmission enhancement compared to that without the reflector (black dash dotted line). The transmission spectrum at peaks

(297.5 kHz, 315.5 kHz, 330.5 kHz, and 340.5 kHz) approaches zero (near-unity transmission). The enhanced transmission efficiency is attributed to the collaborative action of the A_0 -mode reflector, mode converter, and mode selector. Specifically, the forward incident S_0 -mode Lamb wave penetrates the reflector and is partially converted into that in A_0 mode, with the remaining portion being reflected by the mode selector. The reflected S_0 -mode Lamb wave is then reconverted into that in A_0 mode which is subjected to high reflection by the A_0 -mode reflector, rather than being transmitted to the impinged terminal as seen in the UTEM. On the other hand, the introduced reflector has minimal impact on transmission spectrum (<35.8 dB over the frequency band) in the case of backward incidence (blue short dashed line). Figure 8d depicts the out-of-plane displacement at 330.5 kHz, demonstrating a near-complete conversion of the forward-incident S_0 -mode Lamb wave into an A_0 -mode wave, evidenced by the absence of significant standing waves on the left side of the EUTEM (refer to Supplementary Movie 3). Conversely, the backward-induced S_0 -mode Lamb wave encounters difficulty in transmitting through the EUTEM. In line with our proposals for EUTEMs, we have developed an enhanced unidirectional focusing lens (EUFL). The phase modulation mechanism employed in the EUTEM aligns with the concept illustrated in Fig. 4. The EUFL comprises 21 EUTEM units with a focal length of $F = 4\lambda$, where $\lambda = 6.26$ mm denotes the wavelength of the A_0 -mode Lamb wave at 328.5 kHz. Figure 9 illustrates the absolute out-of-plane displacements normalized to the maximal value across various frequencies, which indicates

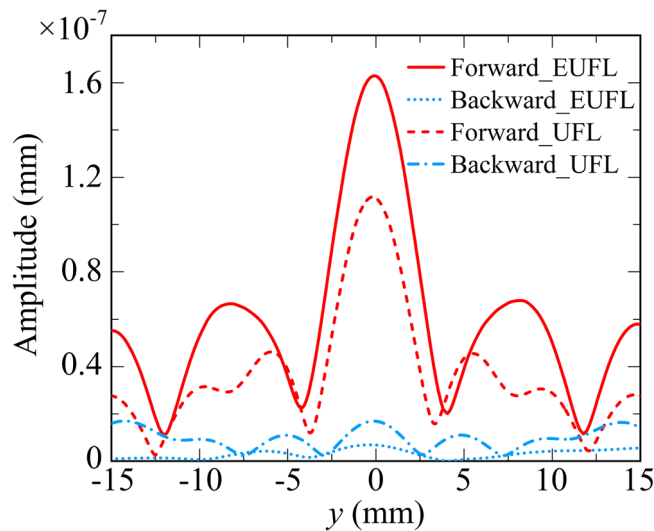


Fig. 10 | Comparison of the focusing performance between the enhanced unidirectional focusing lens (EUFL) and the unidirectional focusing lens (UFL). Out-of-plane displacements of the EUFL (solid line and dotted line) and UFL (short dashed line and dash dotted line) at 315.5 kHz.

that broadband unidirectional focusing is implemented. Moreover, a weakening of displacements on the left side of the EUFL is observed in both forward and backward illumination scenarios compared to those shown in Fig. 6. This hints at a reduction in reflection for forward incidence and improved transmission for backward incidence, enhancing the unidirectional focusing effect. It is suggested that reflection in forward case and transmission in backward case reduces, leading to enhanced unidirectional focusing. We have further analyzed the absolute out-of-plane displacements at 315.5 kHz, as illustrated by the solid line and dotted line in Fig. 10. The forward and backward displacement amplitudes of the EUFL are 1.46 and 0.4 times greater, respectively, than those of the UFL, reaffirming the enhanced unidirectional focusing capability of the EUFL.

Conclusions

To conclude, we have theoretically and experimentally demonstrated unidirectional focusing for broadband Lamb-guided waves based on UTEMs, highlighting their ability for one-way transmission and flexible phase modulation. The UTEM exhibits a significant 30 dB difference in transmission spectra between forward and backward scenarios over the frequency range of 251 kHz to 345.9 kHz, achieved through a combination of Lamb wave conversion and mode selection. The substantial phase velocity contrast between Lamb waves in the S_0 and A_0 modes allows for wide-range phase modulation without compromising the unidirectional effect, achievable solely by adjusting initial positions without altering UTEM geometry or parameters. While the constructed UFL demonstrates sub-wavelength focal sizes for forward-illuminated S_0 -mode Lamb waves, those incident from the opposite side are reflected by the lens. We further propose enhancing forward transmission efficiency by integrating an A_0 -mode reflector into the UTEM. The presented EUTEM shows a <3 dB transmission spectrum from 293.3 kHz to 333.6 kHz, nearing 0 dB at transmission peaks, facilitating a broadband EUFL with improved focus intensity. Due to its scalability and simple configuration, our proposal also provides possibilities to steer higher-frequency broadband Lamb-guided waves on wafer-process-compatible silicon substrates, which paves the way for the development of on-chip elastic devices with substantial versatility.

Data availability

The source data for this work can be found in Supplementary Data 1. All other relevant data that support the findings of this study are available from the corresponding authors upon reasonable request.

Code availability

The simulation code that support the findings of this study is available from the corresponding authors upon reasonable request.

Received: 26 September 2024; Accepted: 6 March 2025;

Published online: 28 March 2025

References

- Yu, N. & Capasso, F. Flat optics with designer metasurfaces. *Nat. Mater.* **13**, 139–150 (2014).
- Xu, Y., Fu, Y. & Chen, H. Planar gradient metamaterials. *Nat. Rev. Mater.* **1**, 1–14 (2016).
- Zheludev, N. I. & Kivshar, Y. S. From metamaterials to metadevices. *Nat. Mater.* **11**, 917–924 (2012).
- Capers, J. R., Boyes, S. J., Hibbins, A. P. & Horsley, S. A. Designing the collective non-local responses of metasurfaces. *Commun. Phys.* **4**, 209 (2021).
- Cummer, S. A., Christensen, J. & Alù, A. Controlling sound with acoustic metamaterials. *Nat. Rev. Mater.* **1**, 1–13 (2016).
- Ma, G. & Sheng, P. Acoustic metamaterials: from local resonances to broad horizons. *Sci. Adv.* **2**, e1501595 (2016).
- Kaina, N., Lemoult, F., Fink, M. & Lerosey, G. Negative refractive index and acoustic superlens from multiple scattering in single negative metamaterials. *Nature* **525**, 77–81 (2015).
- Xie, Y., Popa, B.-I., Zigoneanu, L. & Cummer, S. A. Measurement of a broadband negative index with space-coiling acoustic metamaterials. *Phys. Rev. Lett.* **110**, 175501 (2013).
- Xie, Y. et al. Wavefront modulation and subwavelength diffractive acoustics with an acoustic metasurface. *Nat. Commun.* **5**, 5553 (2014).
- Díaz-Rubio, A. & Tretyakov, S. A. Acoustic metasurfaces for scattering-free anomalous reflection and refraction. *Phys. Rev. B* **96**, 125409 (2017).
- García-Chocano, V. M., Christensen, J. & Sánchez-Dehesa, J. Negative refraction and energy funneling by hyperbolic materials: an experimental demonstration in acoustics. *Phys. Rev. Lett.* **112**, 144301 (2014).
- Li, Y., Qi, S. & Assouar, M. B. Theory of metascreen-based acoustic passive phased array. *N. J. Phys.* **18**, 043024 (2016).
- Sukhovich, A. et al. Experimental and theoretical evidence for subwavelength imaging in phononic crystals. *Phys. Rev. Lett.* **102**, 154301 (2009).
- Li, J., Fok, L., Yin, X., Bartal, G. & Zhang, X. Experimental demonstration of an acoustic magnifying hyperlens. *Nat. Mater.* **8**, 931–934 (2009).
- Lu, D. & Liu, Z. Hyperlenses and metalenses for far-field super-resolution imaging. *Nat. Commun.* **3**, 1205 (2012).
- Yu, N. et al. Light propagation with phase discontinuities: generalized laws of reflection and refraction. *Science* **334**, 333–337 (2011).
- Ramalho, G. M., Lopes, A. M. & da Silva, L. F. Structural health monitoring of adhesive joints using lamb waves: a review. *Struct. Control Health Monit.* **29**, e2849 (2022).
- Lee, G. et al. Piezoelectric energy harvesting using mechanical metamaterials and phononic crystals. *Commun. Phys.* **5**, 94 (2022).
- Jiang, S. et al. Flexible metamaterial electronics. *Adv. Mater.* **34**, 2200070 (2022).
- Zhu, H. & Semperlotti, F. Anomalous refraction of acoustic guided waves in solids with geometrically tapered metasurfaces. *Phys. Rev. Lett.* **117**, 034302 (2016).
- Lee, H., Lee, J. K., Seung, H. M. & Kim, Y. Y. Mass-stiffness substructuring of an elastic metasurface for full transmission beam steering. *J. Mech. Phys. Solids* **112**, 577–593 (2018).
- Liu, Y. et al. Source illusion devices for flexural lamb waves using elastic metasurfaces. *Phys. Rev. Lett.* **119**, 034301 (2017).
- Li, B. et al. Efficient asymmetric transmission of elastic waves in thin plates with lossless metasurfaces. *Phys. Rev. Appl.* **14**, 054029 (2020).

24. Hu, Y. et al. Realization of ultrathin waveguides by elastic metagratings. *Commun. Phys.* **5**, 62 (2022).
25. Zhang, J. et al. Vibration control of flexural waves in thin plates by 3d-printed metasurfaces. *J. Sound Vib.* **481**, 115440 (2020).
26. Xu, Y., Cao, L. & Yang, Z. Deflecting incident flexural waves by nonresonant single-phase meta-slab with subunits of graded thicknesses. *J. Sound Vib.* **454**, 51–62 (2019).
27. Tian, Z. & Yu, L. Elastic phased diffraction gratings for manipulation of ultrasonic guided waves in solids. *Phys. Rev. Appl.* **11**, 024052 (2019).
28. Wang, W., Bonello, B., Djafari-Rouhani, B., Pennec, Y. & Zhao, J. Double-negative pillared elastic metamaterial. *Phys. Rev. Appl.* **10**, 064011 (2018).
29. Cao, L. et al. Disordered elastic metasurfaces. *Phys. Rev. Appl.* **13**, 014054 (2020).
30. Cao, L. et al. Pillared elastic metasurface with constructive interference for flexural wave manipulation. *Mech. Syst. Signal Process.* **146**, 107035 (2021).
31. Jin, Y., Wang, W., Khelif, A. & Djafari-Rouhani, B. Elastic metasurfaces for deep and robust subwavelength focusing and imaging. *Phys. Rev. Appl.* **15**, 024005 (2021).
32. Tol, S., Degertekin, F. & Erturk, A. 3d-printed phononic crystal lens for elastic wave focusing and energy harvesting. *Addit. Manuf.* **29**, 100780 (2019).
33. Huang, S. L., Sun, H. Y., Wang, Q., Wang, S. & Zhao, W. Unidirectional focusing of horizontally polarized shear elastic waves electromagnetic acoustic transducers for plate inspection. *J. Appl. Phys.* **125**, 164504 (2019).
34. Qian, J. et al. Broadband integrative acoustic asymmetric focusing lens based on mode-conversion meta-atoms. *Appl. Phys. Lett.* **116**, 223505 (2020).
35. Xia, J.-P. et al. Broadband tunable acoustic asymmetric focusing lens from dual-layer metasurfaces. *Phys. Rev. Appl.* **10**, 014016 (2018).
36. Tol, S., Degertekin, F. L. & Erturk, A. Phononic crystal Luneburg lens for omnidirectional elastic wave focusing and energy harvesting. *Appl. Phys. Lett.* **111**, 013503 (2017).
37. Stojanoska, K. & Shen, C. Non-Hermitian planar elastic metasurface for unidirectional focusing of flexural waves. *Appl. Phys. Lett.* **120**, 241701 (2022).
38. Xu, K., Ta, D., Su, Z. & Wang, W. Transmission analysis of ultrasonic lamb mode conversion in a plate with partial-thickness notch. *Ultrasonics* **54**, 395–401 (2014).
39. Rose, J. L. *Ultrasonic Guided Waves in Solid Media* (Cambridge University Press, 2014).
40. Su, Z. & Ye, L. *Identification of Damage Using Lamb Waves* (Springer, 2009).
41. Marilyne, P., Kui, Y., Matthieu, G. & Constantinos, S. Lamb waves-based technologies for structural health monitoring of composite structures for aircraft applications. *Eur. J. Mat.* **2**, 436–474 (2022).

Acknowledgements

This work is supported by the National Key R&D Program of China (Grant No. 2022YFA1404400), NSFC (Grant Nos. 12374438, 12225408 and 12227809)

and the Natural Science Foundation of Jiangsu Province (BK20240061 and BK20233001).

Author contributions

H.L. and Y.C. conceived the original idea. H.Z. and H.L. performed the numerical simulation. H.Z., W.L., and X.Z. carried out the experiments and analyzed the data. H.Z., H.L. and Y.C. wrote the original draft and all other authors reviewed and edited it. Y.C. and X.L. supervised the project. All authors contributed to scientific discussions and modifications of the manuscript.

Competing interests

The authors declare no competing interests.

Additional information

Supplementary information The online version contains supplementary material available at

<https://doi.org/10.1038/s42005-025-02032-1>.

Correspondence and requests for materials should be addressed to Houyou Long, Ying Cheng or Xiaojun Liu.

Peer review information *Communications Physics* thanks Yu-Gui Peng, Xinhua Wen and the other, anonymous, reviewer(s) for their contribution to the peer review of this work. A peer review file is available.

Reprints and permissions information is available at <http://www.nature.com/reprints>

Publisher's note Springer Nature remains neutral with regard to jurisdictional claims in published maps and institutional affiliations.

Open Access This article is licensed under a Creative Commons Attribution-NonCommercial-NoDerivatives 4.0 International License, which permits any non-commercial use, sharing, distribution and reproduction in any medium or format, as long as you give appropriate credit to the original author(s) and the source, provide a link to the Creative Commons licence, and indicate if you modified the licensed material. You do not have permission under this licence to share adapted material derived from this article or parts of it. The images or other third party material in this article are included in the article's Creative Commons licence, unless indicated otherwise in a credit line to the material. If material is not included in the article's Creative Commons licence and your intended use is not permitted by statutory regulation or exceeds the permitted use, you will need to obtain permission directly from the copyright holder. To view a copy of this licence, visit <http://creativecommons.org/licenses/by-nc-nd/4.0/>.

© The Author(s) 2025